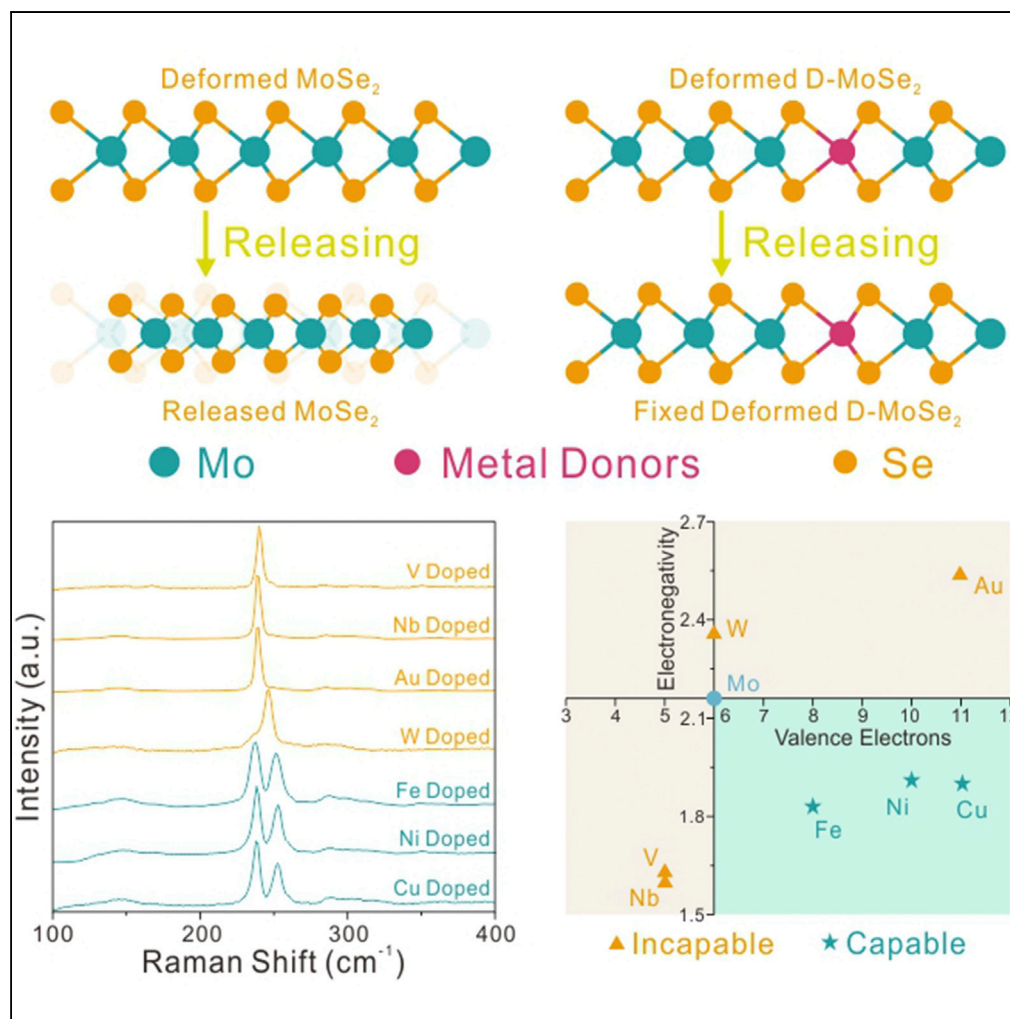## Article

Regulation of Two-Dimensional Lattice Deformation Recovery

Jinxin Liu, Lu Zhou,
Ke Huang, ...,
Xiangheng Xiao,
Mark H. Rümmeli,
Lei Fu

leifu@whu.edu.cn

HIGHLIGHTS

Regulation of the
deformation recovery of
2D lattices by doping
metal donors

Achieving 2D MoSe$_2$ with
uniformly and
permanently stabilized
lattice deformation

Demonstration of the
efficient
micromanipulation of
strict 2D lattices

iScience

Article

Regulation of Two-Dimensional Lattice Deformation Recovery

Jinxin Liu,[1,7] Lu Zhou,[2,7] Ke Huang,[1] Xianyin Song,[3] Yunxu Chen,[1] Xiaoyang Liang,[1] Jin Gao,[4] Xiangheng Xiao,[3] Mark H. Rümmeli,[4,5,6] and Lei Fu[1,2,8,*]

SUMMARY

The lattice directly determines the electronic structure, and it enables controllably tailoring the properties by deforming the lattices of two-dimensional (2D) materials. Owing to the unbalanced electrostatic equilibrium among the dislocated atoms, the deformed lattice is thermodynamically unstable and would recover to the initial state. Here, we demonstrate that the recovery of deformed 2D lattices could be directly regulated via doping metal donors to reconstruct electrostatic equilibrium. Compared with the methods that employed external force fields with intrinsic instability and nonuniformity, the stretched 2D molybdenum diselenide ($MoSe_2$) could be uniformly retained and permanently preserved via doping metal atoms with more outermost electrons and smaller electronegativity than Mo. We believe that the proposed strategy could open up a new avenue in directly regulating the atomic-thickness lattice and promote its practical applications based on 2D crystals.

INTRODUCTION

The lattice of a crystal is its most critical characteristic for determining the electronic structure and further enables controllably tailoring the performed properties (Lee et al., 2005; Weiss, 2010). There is sustained blooming of lattice deformation technology in the broad-range fields of electronics (Zhu et al., 2015; Wu et al., 2014), optics (Wu et al., 2016), magnetics (Levy et al., 2010), catalysis (Li et al., 2016), and energy conversion (Feng et al., 2012). Two-dimensional (2D) materials with great potential of widespread applications (Da et al., 2018; Huang et al., 2018) generally exhibited unique elasticity and flexibility (Frank et al., 2007; Liu et al., 2016), thus providing the most promising platforms to implement the strategy (Zeng et al., 2018; Naumis et al., 2017).

Owing to the unbalanced electrostatic equilibrium of the dislocated atoms, the deformed lattice appears as a thermodynamically unstable system and tends to relax for recovering the intrinsic structural parameters (Zhang et al., 2016). Balancing the additional inner electrostatic interaction requires persistent import of extra energy for suppressing the recovery (Conley et al., 2013; Hui et al., 2013). Consumed approaches in the previous works generally employed external force delivered by the substrates (Ahn et al., 2017; Yan et al., 2013; Li et al., 2015), in view of the great toughness in directly regulating the deformation recovery of atomic-thickness lattices. Therefore the present methods suffer from the intrinsic drawbacks of instability (Feng et al., 2017) and nonuniformity (Liu et al., 2014) of the deformed lattices that are inherited from these force fields.

Here, we demonstrate that the recovery of deformed 2D lattices could be directly regulated by doping metal donors. Metal atom dopants are employed as electron donors to provide extra electrons for reconstructing electrostatic equilibrium among the dislocated atoms. The recovery could be eliminated for achieving lattices with uniformly stabilized and permanently preserved deformation. In this regime, the thermally expanded and *in situ* elastically bent atomic molybdenum diselenide ($MoSe_2$) lattices could be successfully maintained by doping metal donors, which are atoms owning more outermost electrons and smaller electronegativity than Mo, such as iron (Fe) and copper (Cu). We believe that the metal-donor doping (MDD) strategy could open up a new avenue in directly manipulating the 2D lattices and promote its practical applications based on 2D crystals.

RESULTS AND DISCUSSION

Regulation of the Deformation Recovery via Doping Metal Donors

Figure 1A schematically shows the MDD strategy for regulating of $MoSe_2$ lattice deformation recovery via doping metal donors. To investigate the proposition, experiments based on two kinds of metal-doping

[1]College of Chemistry and Molecular Sciences, Wuhan University, Wuhan 430072, China

[2]Institute for Advanced Studies, Wuhan University, Wuhan 430072, China

[3]Department of Physics and Key Laboratory of Artificial Micro and Nanostructures of Ministry of Education, Hubei Nuclear Solid Physics Key Laboratory and Center for Ion Beam Application, Wuhan University, Wuhan 430072, China

[4]College of Physics, Optoelectronics and Energy & Collaborative Innovation Center of Suzhou, Nano Science and Technology, Soochow University, Suzhou 215006, China

[5]Leibniz Institute for Solid State and Materials Research Dresden, P.O. Box 270116, Dresden 01069, Germany

[6]Centre of Polymer and Carbon Materials, Polish Academy of Sciences, M. Curie-Sklodowskiej 34, Zabrze 41-819, Poland

[7]These authors contributed equally

[8]Lead Contact

*Correspondence: leifu@whu.edu.cn

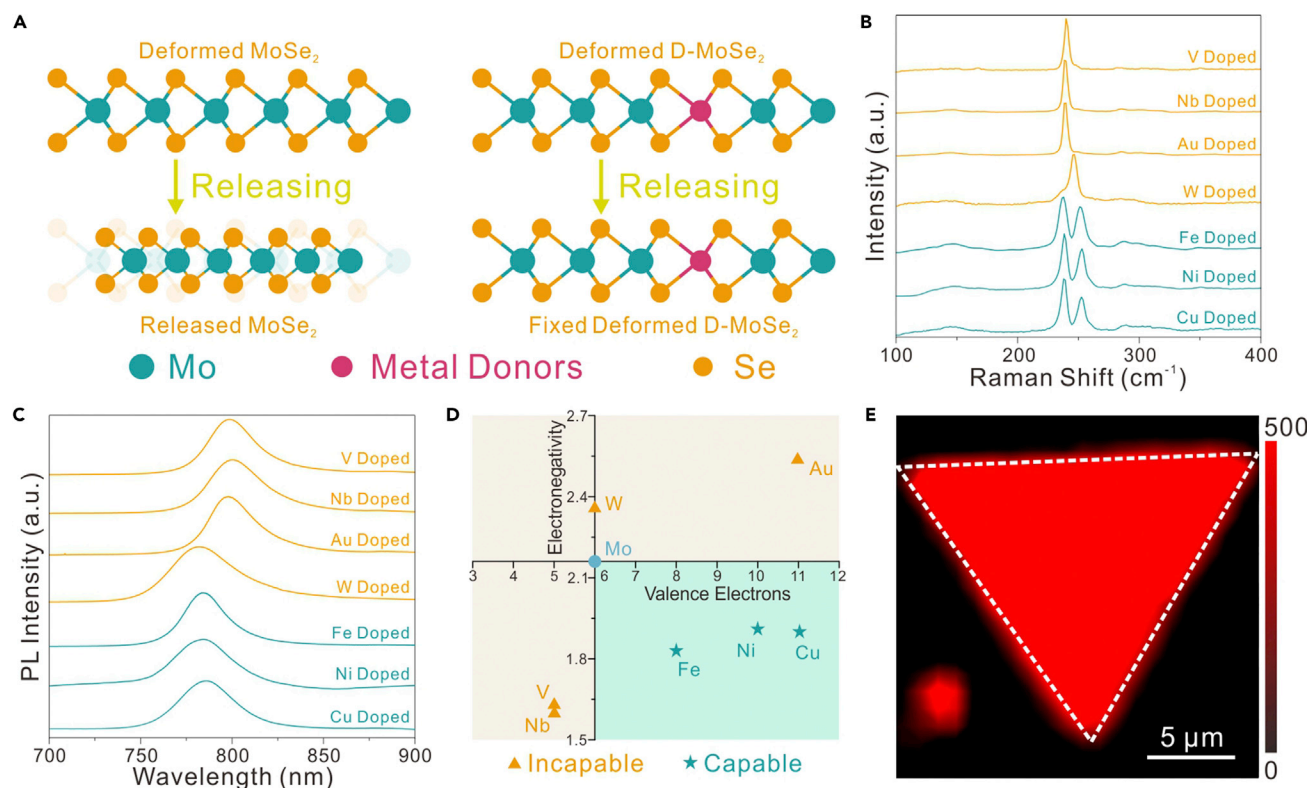https://doi.org/10.1016/j.isci.2019.02.025

Figure 1. Regulation of the Deformation Recovery by Doping Metal Donors

(A) Schematic illustration of the MDD strategy.

(B and C) The Raman spectra (B) and PL spectra (C) of monolayer $MoSe_2$ crystals with various metal dopants.

(D) The plot of the electronegativity and valence electrons of these atoms and their capability to regulate the deformation recovery.

(E) The Raman mapping of a $D-MoSe_2$ crystal.

systems are carried out. The one is the metal-donor system including Fe, nickel (Ni) and Cu atoms, which featured more outermost electrons and smaller electronegativity than Mo atom. The other one is the metal-acceptor system including vanadium (V), niobium (Nb), gold (Au), and tungsten (W) atoms. The employed crystals are directly grown on liquid glass surface via chemical vapor deposition method (Xu et al., 2018; Ju et al., 2017), whereas a corresponding metal foil is utilized as the supporting substrate and the dopant source. During growth, the formed $MoSe_2$ lattices are thermally expanded at the elevated temperature. The donor atoms doped in the deformed lattice could offer extra electrons to modify the electrostatic equilibrium. As a result, the thermal contraction of the donor-doped $MoSe_2$ (D-$MoSe_2$) lattice in the cooling process is inhibited owing to the improved electrostatic repulsion between the bonded atoms, thus realizing the regulation of deformation recovery. The Raman spectra of the as-obtained D-$MoSe_2$ crystals exhibit a split of A_{1g} in Figure 1B, which is in line with the stretched effect of $MoSe_2$ crystals along the c axis (out of plane) (Yasuda et al., 2017). The results of other doping systems exhibit intrinsic Raman features (Gong et al., 2016), and it states the recovery of lattice expansion, thus demonstrating the proposition. The corresponding photoluminescence (PL) spectra (Figure 1C) of D-$MoSe_2$ exhibit an obvious blue shift of the peak position compared with that of pristine $MoSe_2$ crystals (Gong et al., 2016), whereas the spectra acquired in the other doping system are not. It is also thought to be caused by the preserved lattice expansion along all three dimensions of D-$MoSe_2$. Notably, the variation of Raman and PL peaks of the W-doped $MoSe_2$ crystal lines in the alloying effect of $MoSe_2$ and tungsten diselenide (WSe_2) (Xie, 2015), owing to their positions, are all located at the intermediate area between of pristine $MoSe_2$ and pristine WSe_2 (Liu et al., 2016). As plotted in Figure 1D, only the metal atoms located at the fourth quadrant could serve as powerful electron donors in $MoSe_2$ to regulate the deformation recovery, thus demonstrating the proposed mechanism.

For investigating the uniformity of the MDD approach, the characteristic homogeneity of the D-$MoSe_2$ crystals is probed. Taking the Fe-doped $MoSe_2$ as an example, the Raman mapping of one A_{1g} mode at ~237 cm^{-1} of
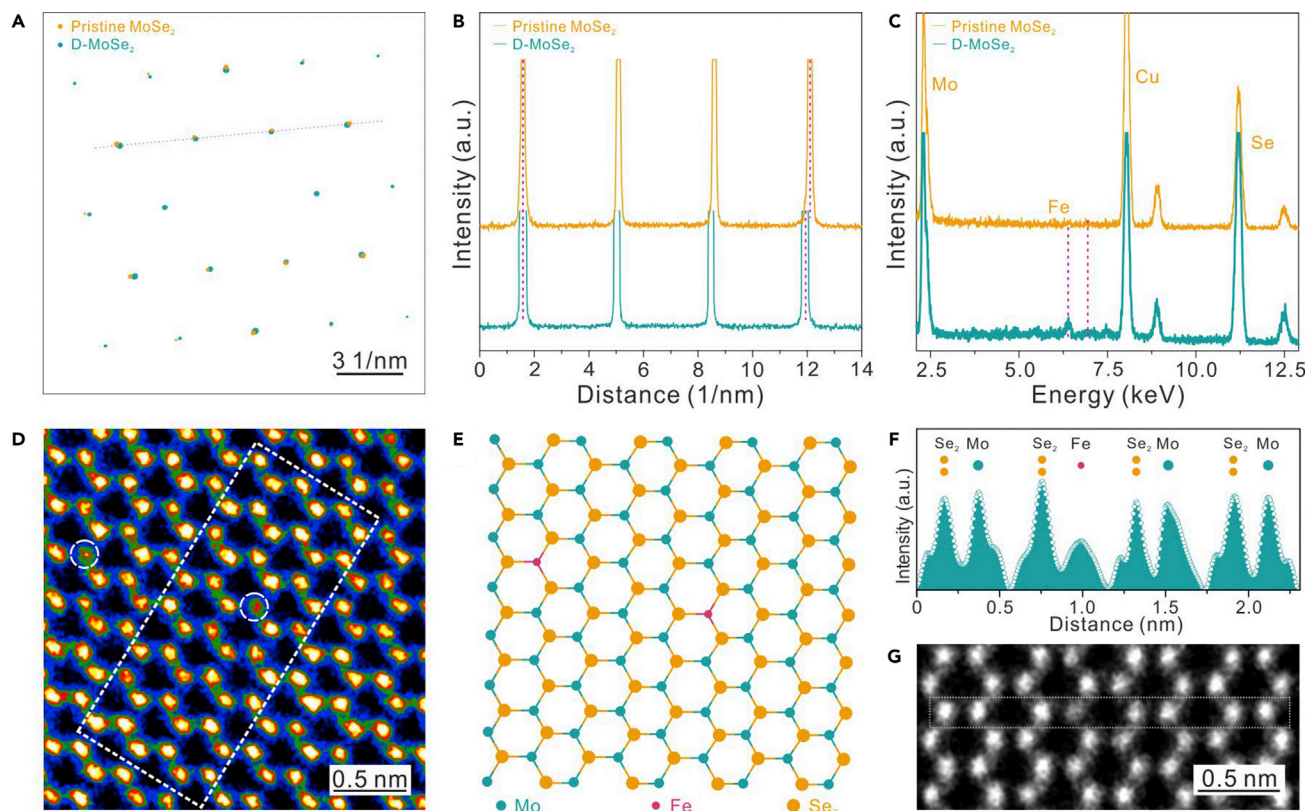
Figure 2. Atomic-Scale Investigations of Regulated D-MoSe2 Crystals

(A) SAED patterns of the pristine $MoSe_2$ and D-$MoSe_2$ crystals.

(B) The corresponding profiles of the line marked in (A).

(C) The EDX spectra of the two samples.

(D) The false-color HAADF-STEM image of the D-$MoSe_2$ crystal.

(E) The simulated atom structure of (D).

(F) The line profile of the atoms highlighted in (G).

(G) The corresponding Z-contrast image of the marked area in (D).

a triangle is presented (Figure 1E), where the uniform intensity over the whole crystal indicated the uniform regulation effect in a certain crystal. The corresponding optical microscopic image and PL mapping (Figure S1) also present a uniform contrast. Statistical analyses of the Raman peak difference between the two split A_{1g} peaks and the PL peak position of 100 randomly selected D-$MoSe_2$ single crystals on the same substrate further demonstrate the homogeneity (Figure S1). We notice that the split of A_{1g} peak of monolayer $MoSe_2$ crystals can also be caused by the S alloying (Feng et al., 2015) or Se vacancy (Mahjouri-Samani et al., 2016), which is denied by X-ray photoelectron spectroscopy (XPS) measurements, therefore no peak assigned to S element is detected (Figure S2) and the atomic ratio of Mo/Se is verified as 0.98 (Figure S3). It also suggested a doping level of ∼2%. Furthermore, the metal doping and monolayer nature of the crystal are also confirmed by XPS (Figure S3) and AFM measurements (Figure S4).

Atomic-Scale Investigations of Regulated D-MoSe$_2$ Crystals

The MDD strategy enables the transfer of the crystals with preserved lattice deformation on the Cu grids. The characterizations of the as-grown monolayer D-$MoSe_2$ crystals on the atomic scale are then probed by the transmission electron microscope (TEM) (Figure S5). Selected area electron diffraction (SAED) of the doped and pristine crystal is performed to evaluate the regulation of lattice deformation recovery. The obtained results (Figure 2A) suggest the different repeating intervals between two sets of SAED patterns, further revealing distinct lattice structures (Ahn et al., 2017). For the (100) planes, the separation distance between the diffraction points of the pristine crystal is longer than that of the MDD one (Figure 2B), which indicates a ∼101.5% times extension of the D-$MoSe_2$ lattice. Notably, the microscope parameters camera
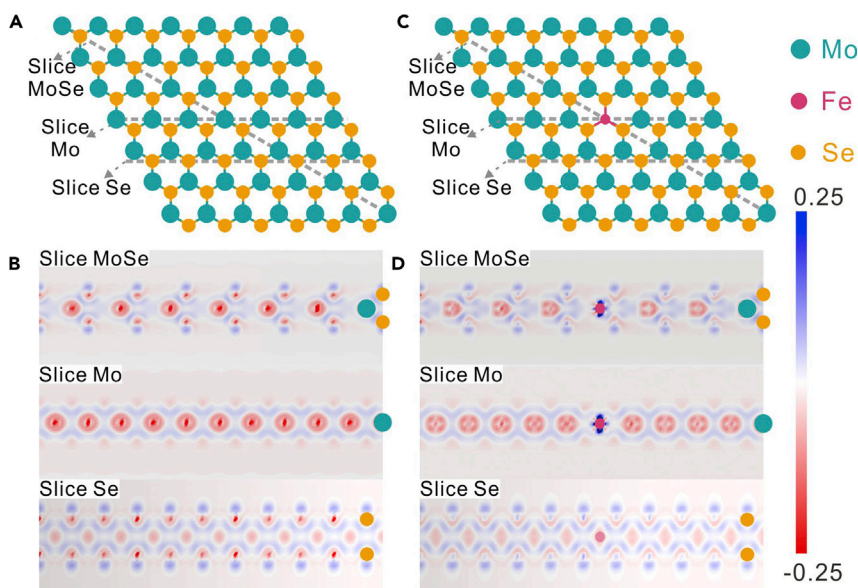
Figure 3. Theoretical Calculations of the MDD Effect

(A and C) The top-view illustration of the analyzed pristine 7×7 $MoSe_2$ crystal (A) and D-$MoSe_2$ crystal (C).

(B and D) The corresponding isosurface images of the pristine $MoSe_2$ (B) and D-$MoSe_2$ (D) slices of the positions marked in (A) and (C), respectively.

length and lens aberrations are set as constant values for all subsequent measurements to ensure the reliability of the contrast experiments. The high-resolution TEM images of the two samples and the corresponding fast Fourier transformation patterns are also presented for further comparisons (Figure S6). The results also indicate similar observations of ~1.5% persevered deformation for the doped lattice. The TEM-based energy dispersive X-ray (EDX) spectroscopy is employed to affirm the presence of Fe element, as displayed in Figure 2C. Here, the Cu element is contributed by the Cu grids.

High-angle annular dark-field scanning transmission electron microscopy (HAADF-STEM) is also employed to probe the doping site of D-$MoSe_2$ crystal at the atomic scale. The false-color Z-contrast image displayed in Figure 2D presents the typical atomic arrangement of $MoSe_2$ crystal bonding with several heteroatoms (marked by circles), in which the Mo and Se_2 sites exhibit similar intensity contrast in the HAADF measurement (Huang et al., 2014; Feng et al., 2014). The as-marked heteroatom sites manifest a weaker intensity compared with the surroundings, and they are believed to be the metal donor atoms that replaced the Mo sites, owing to the smaller atomic number of Fe (26) than Mo (42). The simulated atom structure (Figure 2E) illustrates a typical D-$MoSe_2$ lattice architecture. The line profile (Figure 2F) of the relative contrast of the atoms highlighted in Figure 2G (the region marked in Figure 2D) suggests a visible intensity difference between the doped atom and Se_2 or Mo atoms with a ratio of ~0.4, which is close to the theoretically calculated value of 0.45 (Krivanek et al., 2010), thus further affirming the presence of Fe atoms. The theoretical intensity ratio between Se and Mo is 0.71, which is lower than the obtained value of ~0.4, further excluding the presence of Se vacancy. Moreover, the geometric phase analysis (GPA) based on HAADF-STEM image is also performed to evaluate the uniformity at atomic scale. The results presented in Figure S7 reveal a homogeneous geometric phase over the whole region (Han et al., 2018; Xie et al., 2018), which intuitively demonstrates the uniformity of MDD strategy. Based on all these high-resolution structural characterizations, the bonding of metal donor atoms via substitution at Mo sites as well as the uniformly regulated deformation recovery of the lattice with ~1.5% preservation is suggested (Figure S8).

Theoretical Calculations of the MDD Effect

The MDD effect is directly evaluated by the charge density difference based on the density functional theory (DFT) calculations (Yang et al., 2013). $MoSe_2$ crystal structure with 7 × 7 × 1 cell size is constructed for simulation, whereas a doping level of ~2% could be obtained by replacing one Mo atom by Fe atom.
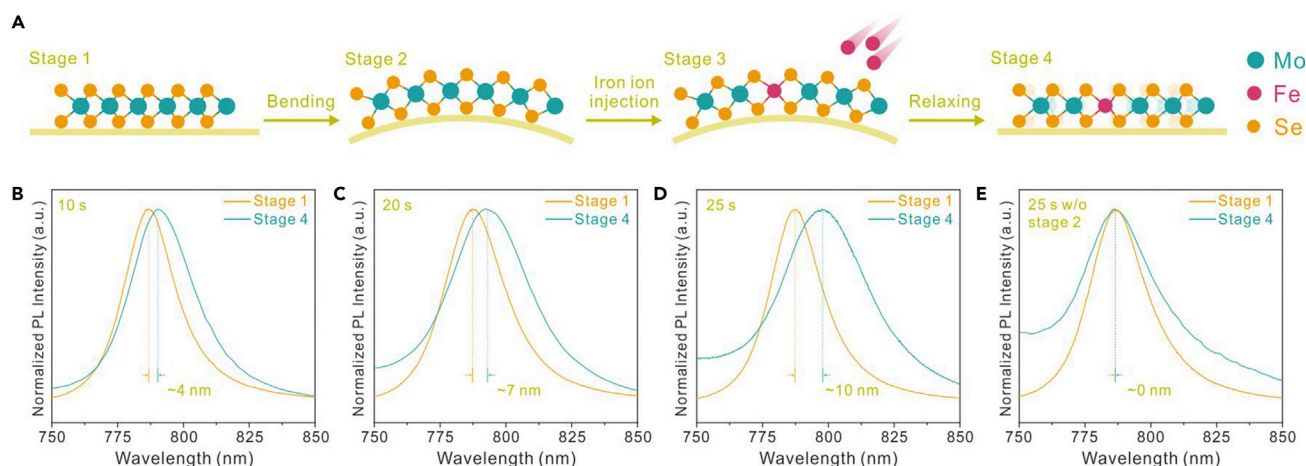
Figure 4. *In Situ* Investigations of the MDD Strategy

(A) Schematic illustration of the *in situ* strategy.

(B–D) The PL spectra acquired from the corresponding monolayer crystals at stage 1 (yellow line) and stage 4 (cyan line) for injecting Fe ions for 10 s (B), 20 s (C), and 25 s (D) in stage 3.

(E) PL spectra of a MoSe$_2$ crystal transferred on PET film (yellow line) and after injecting Fe ions for 25 s without bending the substrate (cyan line).

The top view of pristine MoSe$_2$ crystal is illustrated in Figure 3A, and the corresponding charge density difference slices acquired along the as-marked (110) plane (slice MoSe), the (100) plane of Mo atoms (slice Mo), and the (100) plane of Se atoms (slice Se) are displayed in Figure 3B. The presented isosurfaces indicate a natural electron-trap state (colored by blue) around the Se atoms and electron-loss state (colored by red) around the Mo atoms, which are caused by the electronegativity difference. The scheme of D-MoSe$_2$ crystal and the corresponding isosurfaces are also presented in Figures 3C and 3D for comparison, respectively. Considerable distinctions between two series of slices after the substitution of one atom are exhibited visually. By doping by one metal donor atom, the electron-loss effect (represented by the color intensity of red) of all the Mo atoms is much weaker than the pristine one, whereas that of all the Se atoms at the central region is totally converted into the electron-trap effect (represented by the color intensity of blue). This variation of charge density is believed to be caused by the doping of metal donor, which featured more valence electrons and smaller electronegativity than Mo, thus providing the additional electrons for the lattice and modifying the electrostatic equilibrium among the Mo and Se atoms. For further investigating the scope, the planar charge density difference slices along the side view of two crystals are analyzed and the same results along the entire metal-donor-doped cell could be confirmed (Figure S9). For further confirming the regulation effect of lattice deformation recovery, energy calculations of 7×7 MoSe$_2$ crystals with four configurations are performed (Zhang et al., 2016). As exhibited in Figure S10, the enlarged pristine lattice is thermodynamically unstable and would recover to the original state, whereas the metal-donor-doped lattice would be more stable after expansion and the deformation recovery could be eliminated after a releasing process. These results theoretically illustrate the regulation ability of the lattice deformation recovery based on the MDD strategy.

In Situ Investigations of the MDD Strategy

In situ studies are carried out for directly confirming the regulation ability based on the MDD strategy. As schemed in Figure 4A, pristine monolayer MoSe$_2$ crystals grown on Si/SiO$_2$ substrates are transferred to the flexible polyethylene terephthalate (PET) films (stage 1). Then the lattices are deformed by bending the PET substrates (stage 2). Room temperature Fe-ion injection at 5 keV is performed to form the deformed D-MoSe$_2$ crystals (stage 3) (Song et al., 2018). Finally, the bent PET films are relaxed to the plane configurations for releasing the delivered force field of the crystals (stage 4). Here, compared with the PL features of pristine monolayer MoSe$_2$, an ~15-nm blue shift of the PL peak position for the freshly transferred crystals on PET substrates (stage 1) is presented (Figure S11). Figure 4B displayed the PL acquisitions of a certain MoSe$_2$ crystal on the flat PET substrate before (yellow, at stage 1) and after (cyan, at stage 4) Fe ion injection of 10 s. About 4-nm red shift of the

peak position is observed in the normalized PL spectra of the same crystal. For the prolonged injection durations, the red shifts of the PL peak positions of the corresponding crystals exhibited correspondingly enlarged values, as presented in Figure 4C (20 s for 7 nm) and Figure 4D (25 s for 10 nm). Here, the variation of PL peaks agrees well with the shift tendency of monolayer $MoSe_2$ lattice with in-plane deformation (Horzum et al., 2013), thus directly demonstrating the regulation ability of the lattice deformation recovery based on the MDD strategy. As a contrast test, the *in situ* experiments without stage 2 and injection for 25 s are investigated and no change is presented in PL peaks (Figure 4E), which reveals that directly doping metal donors would not cause the lattice deformation. These results affirm the realization of *in situ* regulating the lattice deformation recovery and further verify the proposed mechanism. However, further lengthening the injection time may deconstruct the crystal structure and eliminate the PL signal (Figure S12), which prevents the next step investigations. More *in situ* results at other stages are also offered in Figure S13, in which the statistical analyses of these PL peak position values demonstrate the same red shift tendency of D-$MoSe_2$ crystals based on the MDD strategy.

Conclusion

In summary, based on the MDD strategy, we achieved permanent and uniform regulation of 2D lattice deformation recovery. Metal donors are employed to offer additional electrons to the lattices and reconstruct the electrostatic equilibrium among the atoms. The expansion of monolayer $MoSe_2$ could be then fixed after doping Fe, Cu, or Ni atoms. The proposition is perfectly confirmed by the theoretical calculations and *in situ* experiments. We believe that the developed strategy will open up a new avenue to directly manipulate the 2D lattice, thus promoting and accelerating the ongoing research efforts as well as practical applications of lattice deformation based on 2D crystals.

Limitations of Study

This work mainly investigates the regulation of 2D lattice deformation recovery by doping metal donors, in which most of the results originated from the Fe-doped samples. More studies need to concentrate on probing the difference brought about by doping different metal donors in the 2D crystals. Exploration of the robustness and the controllability of this strategy also warrants further studies.

METHODS

All methods can be found in the accompanying Transparent Methods supplemental file.

SUPPLEMENTAL INFORMATION

Supplemental Information can be found online at https://doi.org/10.1016/j.isci.2019.02.025.

AUTHOR CONTRIBUTIONS

L.F. developed the concept and conceived the experiments. J.L. and L.Z. carried out the experiments. L.F. and J.L. wrote the manuscript. L.F., J.L., L.Z., K.H., X.S., Y.C., X.L., J.G., X.X., and M.R. contributed to data analysis and scientific discussion.

DECLARATION OF INTERESTS

The authors declare no competing interests.

REFERENCES

Ahn, G.H., Amani, M., Rasool, H., Lien, D.H., Mastandrea, J.P., Ager Iii, J.W., Dubey, M., Chrzan, D.C., Minor, A.M., and Javey, A. (2017). Strain-engineered growth of two-dimensional materials. Nat. Commun. 8, 608.

Conley, H.J., Wang, B., Ziegler, J.I., Haglund, R.F., Jr., Pantelides, S.T., and Bolotin, K.I. (2013). Bandgap engineering of strained monolayer and bilayer MoS₂. Nano Lett. 13, 3626–3630.

Da, Y., Liu, J., Zhou, L., Zhu, X., Chen, X., and Fu, L. (2018). Engineering 2D architectures towards high-performance microsupercapacitors. Adv. Mater. 31, 1802793.

Feng, J., Qian, X., Huang, C.-W., and Li, J. (2012). Strain-engineered artificial atom as a broad-spectrum solar energy funnel. Nat. Photonics 6, 866–872.

Feng, Q., Zhu, Y., Hong, J., Zhang, M., Duan, W., Mao, N., Wu, J., Xu, H., Dong, F., Lin, F., et al. (2014). Growth of large-area 2D MoS₂₍₁₋ₓ₎Se₂ₓ semiconductor alloys. Adv. Mater. 26, 2648–2653.

Feng, Q., Mao, N., Wu, J., Xu, H., Wang, C., Zhang, J., and Xie, L. (2015). Growth of MoS₂₍₁₋ₓ₎Se₂ₓ (x = 0.41-1.00) monolayer alloys with controlled morphology by physical vapor deposition. ACS Nano 9, 7450–7455.

Feng, S., Yang, R., Jia, Z., Xiang, J., Wen, F., Mu, C., Nie, A., Zhao, Z., Xu, B., Tao, C., et al. (2017). Strain release induced novel fluorescence variation in CVD-grown monolayer WS₂ crystals. ACS Appl. Mater. Interfaces 9, 34071–34077.

Frank, I.W., Tanenbaum, D.M., van der Zande, A.M., and McEuen, P.L. (2007). Mechanical properties of suspended graphene sheets. J. Vac. Sci. Technol. B 25, 2558.

Gong, Y., Ye, G., Lei, S., Shi, G., He, Y., Lin, J., Zhang, X., Vajtai, R., Pantelides, S.T., Zhou, W., et al. (2016). Synthesis of millimeter-scale transition metal dichalcogenides single crystals. Adv. Funct. Mater. 26, 2009–2015.

Han, Y., Li, M.Y., Jung, G.S., Marsalis, M.A., Qin, Z., Buehler, M.J., Li, L.J., and Muller, D.A. (2018). Sub-nanometre channels embedded in two-dimensional materials. Nat. Mater. 17, 129–133.

Horzum, S., Sahin, H., Cahangirov, S., Cudazzo, P., Rubio, A., Serin, T., and Peeters, F.M. (2013). Phonon softening and direct to indirect band gap crossover in strained single-layer MoSe₂. Phys. Rev. B 87, 125415.

Huang, C., Wu, S., Sanchez, A.M., Peters, J.J., Beanland, R., Ross, J.S., Rivera, P., Yao, W., Cobden, D.H., and Xu, X. (2014). Lateral heterojunctions within monolayer MoSe₂-WSe₂ semiconductors. Nat. Mater. 13, 1096–1101.

Huang, K., Liu, J., Tan, L., Zuo, J., and Fu, L. (2018). Ultrahigh temperature graphene molecular heater. Adv. Mater. Interfaces 5, 1701299.

Hui, Y.Y., Liu, X., Jie, W., Chan, N.Y., Hao, J., Hsu, Y.T., Li, L.J., Guo, W., and Lau, S.P. (2013). Exceptional tunability of band energy in a compressively strained trilayer MoS₂ sheet. ACS Nano 7, 7126–7131.

Ju, M., Liang, X.Y., Liu, J.X., Zhou, L., Liu, Z., Mendes, R.G., Rummeli, M.H., and Fu, L. (2017). Universal substrate trapping strategy to grow strictly monolayer transition metal dichalcogenides crystals. Chem. Mater. 29, 6095–6103.

Krivanek, O.L., Chisholm, M.F., Nicolosi, V., Pennycook, T.J., Corbin, G.J., Dellby, N., Murfitt, M.F., Own, C.S., Szilagyi, Z.S., Oxley, M.P., et al. (2010). Atom-by-atom structural and chemical analysis by annular dark-field electron microscopy. Nature 464, 571–574.

Lee, M.L., Fitzgerald, E.A., Bulsara, M.T., Currie, M.T., and Lochtefeld, A. (2005). Strained Si, SiGe, and Ge channels for high-mobility metal-oxide-semiconductor field-effect transistors. J. Appl. Phys. 97, 011101.

Levy, N., Burke, S.A., Meaker, K.L., Panlasigui, M., Zettl, A., Guinea, F., Castro Neto, A.H., and Crommie, M.F. (2010). Strain-induced pseudo-magnetic fields greater than 300 tesla in graphene nanobubbles. Science 329, 544–547.

Li, H., Contryman, A.W., Qian, X., Ardakani, S.M., Gong, Y., Wang, X., Weisse, J.M., Lee, C.H., Zhao, J., Ajayan, P.M., et al. (2015). Optoelectronic crystal of artificial atoms in strain-textured molybdenum disulfide. Nat. Commun. 6, 7381.

Li, H., Tsai, C., Koh, A.L., Cai, L., Contryman, A.W., Fragapane, A.H., Zhao, J., Han, H.S., Manoharan, H.C., Abild-Pedersen, F., et al. (2016). Corrigendum: activating and optimizing MoS₂ basal planes for hydrogen evolution through the formation of strained sulphur vacancies. Nat. Mater. 15, 364.

Liu, Z., Amani, M., Najmaei, S., Xu, Q., Zou, X., Zhou, W., Yu, T., Qiu, C., Birdwell, A.G., Crowne, F.J., et al. (2014). Strain and structure heterogeneity in MoS₂ atomic layers grown by chemical vapour deposition. Nat. Commun. 5, 5246.

Liu, J., Cao, H., Jiang, B., Xue, Y., and Fu, L. (2016). Newborn 2D materials for flexible energy conversion and storage. Sci. China Mater. 59, 459–474.

Liu, J., Zeng, M., Wang, L., Chen, Y., Xing, Z., Zhang, T., Liu, Z., Zuo, J., Nan, F., Mendes, R.G., et al. (2016). Ultrafast self-limited growth of strictly monolayer WSe₂ crystals. Small 12, 5741–5749.

Mahjouri-Samani, M., Liang, L., Oyedele, A., Kim, Y.S., Tian, M., Cross, N., Wang, K., Lin, M.W., Boulesbaa, A., Rouleau, C.M., et al. (2016). Tailoring vacancies far beyond intrinsic levels changes the carrier type and optical response in monolayer MoSe₂₋ₓ crystals. Nano Lett. 16, 5213–5220.

Naumis, G.G., Barraza-Lopez, S., Oliva-Leyva, M., and Terrones, H. (2017). Electronic and optical properties of strained graphene and other strained 2D materials: a review. Rep. Prog. Phys. 80, 096501.

Song, X., Li, W., He, D., Wu, H., Ke, Z., Jiang, C., Wang, G., and Xiao, X. (2018). The "midas touch" transformation of TiO₂ nanowire arrays during visible light photoelectrochemical performance by carbon/nitrogen coimplantation. Adv. Energy Mater. 8, 1800165.

Weiss, P. (2010). Straining for speed: in search of faster electronics, chip makers contort silicon crystals. Sci. News 165, 136–138.

Wu, W., Wang, L., Li, Y., Zhang, F., Lin, L., Niu, S., Chenet, D., Zhang, X., Hao, Y., Heinz, T.F., et al. (2014). Piezoelectricity of single-atomic-layer MoS₂ for energy conversion and piezotronics. Nature 514, 470–474.

Wu, W., Wang, L., Yu, R., Liu, Y., Wei, S.H., Hone, J., and Wang, Z.L. (2016). Piezophototronic effect in single-atomic-layer MoS₂ for strain-gated flexible optoelectronics. Adv. Mater. 28, 8463–8468.

Xie, S., Tu, L., Han, Y., Huang, L., Kang, K., Lao, K.U., Poddar, P., Park, C., Muller, D.A., DiStasio, R.A., Jr., et al. (2018). Coherent, atomically thin transition-metal dichalcogenide superlattices with engineered strain. Science 359, 1131–1136.

Xie, L.M. (2015). Two-dimensional transition metal dichalcogenide alloys: preparation, characterization and applications. Nanoscale 7, 18392–18401.

Xu, D., Chen, W., Zeng, M., Xue, H., Chen, Y., Sang, X., Xiao, Y., Zhang, T., Unocic, R.R., Xiao, K., et al. (2018). Crystal-field tuning of photoluminescence in two-dimensional materials with embedded lanthanide ions. Angew. Chem. Int. Ed. 57, 755–759.

Yan, W., He, W.Y., Chu, Z.D., Liu, M., Meng, L., Dou, R.F., Zhang, Y., Liu, Z., Nie, J.C., and He, L. (2013). Strain and curvature induced evolution of electronic band structures in twisted graphene bilayer. Nat. Commun. 4, 2159.

Yang, X.H., Fu, H.T., Wong, K., Jiang, X.C., and Yu, A.B. (2013). Hybrid Ag@TiO₂ core-shell nanostructures with highly enhanced photocatalytic performance. Nanotechnology 24, 415601.

Yasuda, S., Takahashi, R., Osaka, R., Kumagai, R., Miyata, Y., Okada, S., Hayamizu, Y., and Murakoshi, K. (2017). Out-of-plane strain induced in a moire superstructure of monolayer MoS₂ and MoSe₂ on Au(111). Small 13, 1700748.

Zeng, M., Xiao, Y., Liu, J., Yang, K., and Fu, L. (2018). Exploring two-dimensional materials toward the next-generation circuits: from monomer design to assembly control. Chem. Rev. 118, 6236–6296.

Zhang, Q., Chang, Z., Xu, G., Wang, Z., Zhang, Y., Xu, Z.-Q., Chen, S., Bao, Q., Liu, J.Z., Mai, Y.-W., et al. (2016). Strain relaxation of monolayer WS₂ on plastic substrate. Adv. Funct. Mater. 26, 8707–8714.

Zhang, T., Jiang, B., Xu, Z., Mendes, R.G., Xiao, Y., Chen, L., Fang, L., Gemming, T., Chen, S., Rummeli, M.H., et al. (2016). Twinned growth behaviour of two-dimensional materials. Nat. Commun. 7, 13911.

Zhu, H., Wang, Y., Xiao, J., Liu, M., Xiong, S., Wong, Z.J., Ye, Z., Ye, Y., Yin, X., and Zhang, X. (2015). Observation of piezoelectricity in free-standing monolayer MoS₂. Nat. Nanotechnol. 10, 151–155.

Supplemental Information

Regulation of Two-Dimensional Lattice

Deformation Recovery

Jinxin Liu, Lu Zhou, Ke Huang, Xianyin Song, Yunxu Chen, Xiaoyang Liang, Jin Gao, Xiangheng Xiao, Mark H. Rümmeli, and Lei Fu
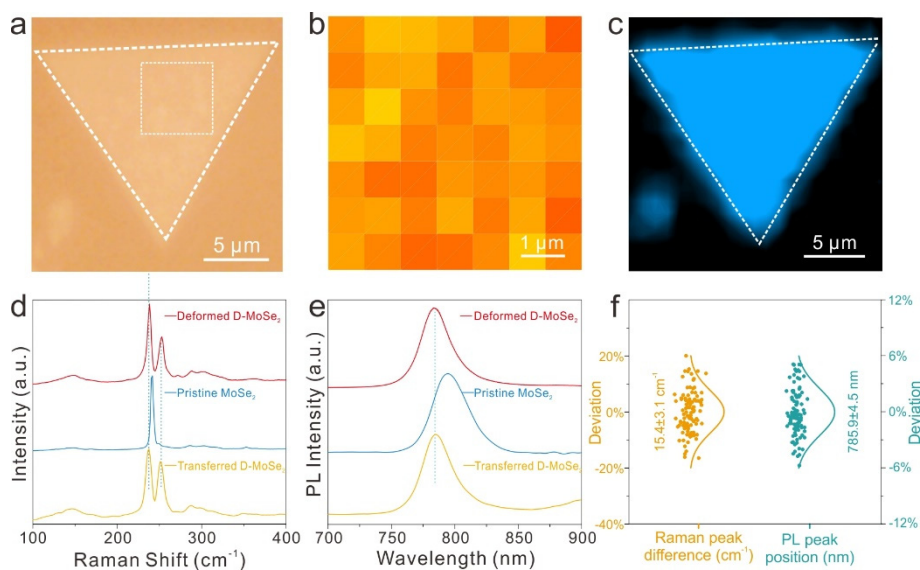
Figure S1. (a) The OM image of the as-grown monolayer D-MoSe$_2$ single crystal on the glass substrate. (b) The plot of the peak difference of split Raman A$_{1g}$ peaks acquired from the crystal area marked in (a). (c) PL mapping at 784 nm of the crystal in (a). (d) Raman spectra and (e) PL spectra acquired from the deformed D-MoSe$_2$ crystal (red line), pristine MoSe$_2$ crystal (blue line), and transferred deformed D-MoSe$_2$ crystal (yellow line). (f) The statistical analysis of the Raman peak difference between the two split A$_{1g}$ peaks and PL peak position of 100 randomly selected D-MoSe$_2$ single crystals on the same substrate.

A typical OM image of the as-grown monolayer donor-doped MoSe$_2$ (D-MoSe$_2$) crystal is displayed in Figure S1a, which presents a uniform contrast of the triangle. The Raman acquisitions of a zoom-in area, which is marked in Figure S1a by a square, are acquired to further investigate the homogeneity in detail. The resulting plot in Figure S1b exhibited little difference in color intensity, which represents the Raman peak difference of the corresponding crystal area and illustrates the uniform fixing effect (from 15 cm^{-1} to 17 cm^{-1}). The corresponding photoluminescence (PL) mapping at ~784 nm is presented in Figure S1c and the uniform intensity over the whole crystal indicates the uniformly preserved lattice deformation of the D-MoSe$_2$ crystal. The Raman spectrum of deformed D-MoSe$_2$ (red line of Figure S1d) exhibits a split of A$_{1g}$ peak, which is in line with the stretch effect of MoSe$_2$ crystals along the c axis (out of plane), further proving the thermal expansion as the only cause. Otherwise, the Raman spectrum of the pristine MoSe$_2$ (blue line of Figure S1d) exhibited the typical characteristics of intrinsic MoSe$_2$ crystals, indicating the elimination of thermally expanding effect in the un-doped one. For further excluding the influence of substrate, the deformed D-MoSe$_2$ are transferred to the Si/SiO$_2$ substrate and the Raman spectrum remain unchanged (yellow line of Figure S1d), thus demonstrating the regulation effect of MDD. The corresponding PL spectra are presented in Figure S1e and also present similar behaviors. For investigating the uniformity of the metal-donor doping (MDD) strategy, a statistical analysis of the Raman peak difference between the two split A$_{1g}$ peaks and PL peak position of 100 randomly selected D-MoSe$_2$ single crystals on the same substrate was carried out (Figure S1f). The standard deviations of the peak differences and the peak positions are only 3.1 cm^{-1} and 4.5 nm, respectively, and the corresponding average values are 15.4 cm^{-1} and 785.9 nm, respectively. The statistics indicate a uniform regulation of the lattice deformation recovery over the whole substrate.
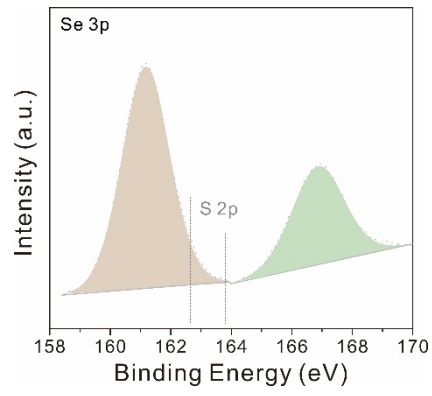
Figure S2. The XPS spectrum of the transferred D-MoSe$_2$ crystals for Se 3p peaks. No obvious peaks related to the S 2p components of MoS$_2$[1] or MoS$_x$Se$_{2-x}$[2,3] is detected.
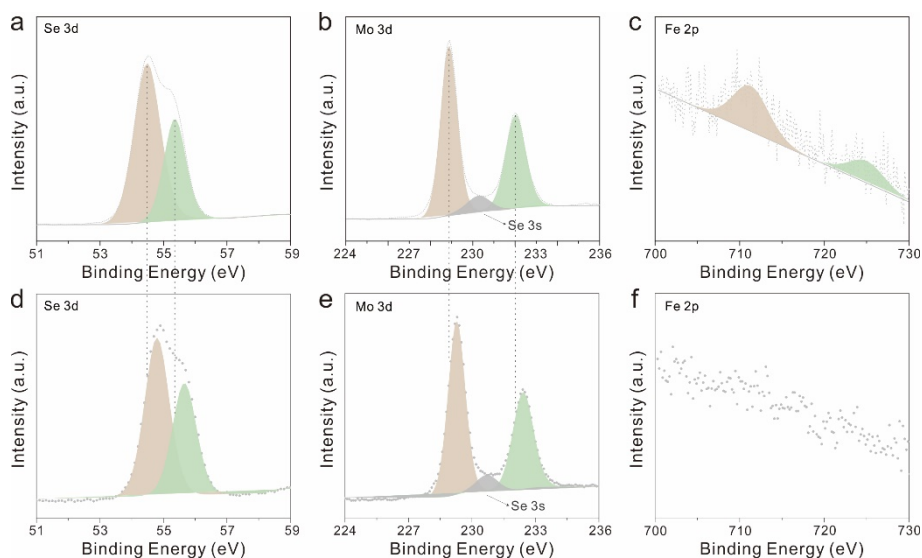
Figure S3. The XPS spectra of the transferred D-MoSe$_2$ crystals for (a) Se 3d peaks, (b) Mo 3d peaks, and (c) Fe 2p peaks. The XPS spectra of the as-grown pristine MoSe$_2$ crystals for (d) Se 3d peaks, (e) Mo 3d peaks, and (f) Fe 2p peaks.

Figure S3 indicates the presence of metal donor elements in the D-MoSe$_2$ crystals. The calculated Mo/Se atomic ratio is about 0.49 and this result reveals the inexistence of Se vacancy and the doping level of about 2%. Moreover, compared with the Se 3d peaks and Mo 3d peaks recorded from pristine MoSe$_2$ crystals, the peaks of the D-MoSe$_2$ crystals exhibit an obviously left shift, which is caused by the lattice deformation.[4]
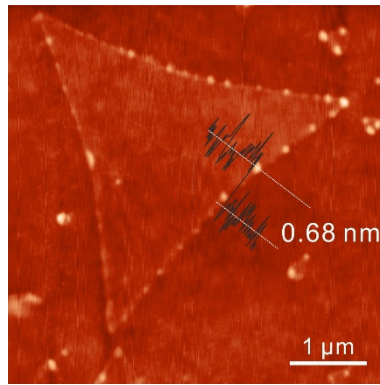
Figure S4. AFM image of the D-MoSe$_2$ crystal with the thickness of ~0.68 nm, which is consisted with the value of monolayer MoSe$_2$ crystal[5].
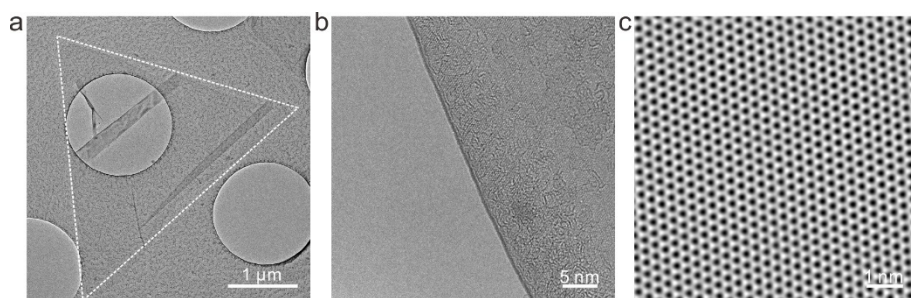
Figure S5. (a) Low magnification TEM image of the monolayer D-MoSe$_2$ crystal. (b) Edge analysis of the crystal, where the single black line indicates the monolayer nature of the crystal. (c) A typical HRTEM image of the crystal, which indicates the high crystallinity of it.
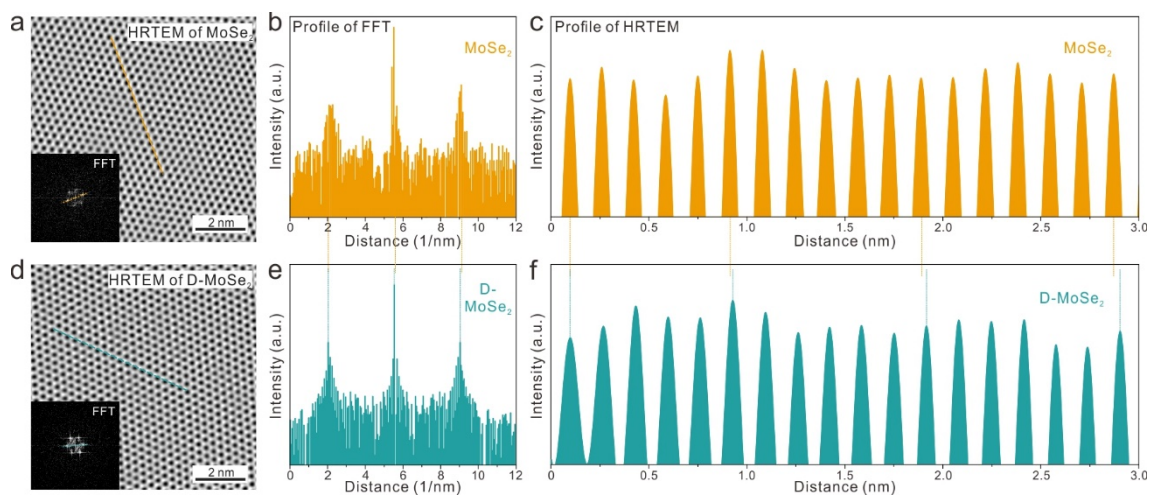
Figure S6. The HRTEM images of (a) the pristine MoSe$_2$ crystal and (d) the D-MoSe$_2$ crystal. Inset presented the corresponding fast Fourier transformation (FFT) patterns. The profiles of the (b, e) FFT patterns and (c, f) the HRTEM images of the two crystals are presented respectively. The results further demonstrate the elimination of lattice deformation recovery of the D-MoSe$_2$ crystal based on the MDD strategy.
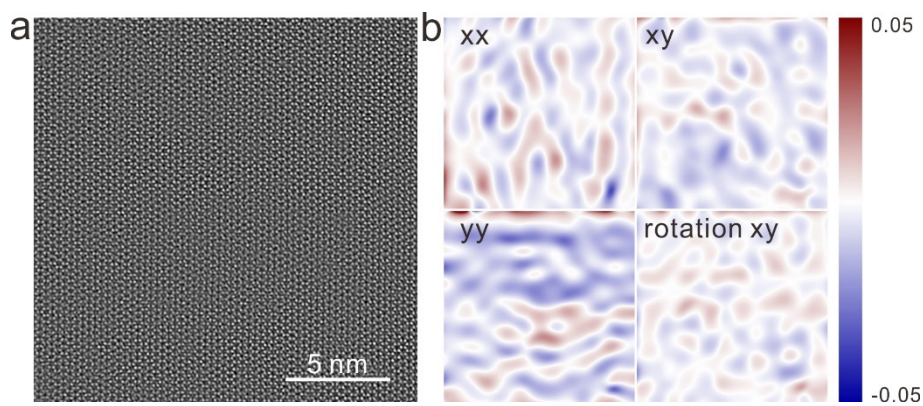
Figure S7. (a) The high-angle annular dark field scanning transmission electron microscopy (HAADF-STEM) image of the D-MoSe₂ crystal. (b) The corresponding geometric phase analysis images. The results reveal a homogeneous geometric phase over the whole region and it indicates no obvious distinct structural deformation is generated, further demonstrating the uniform regulation effect.
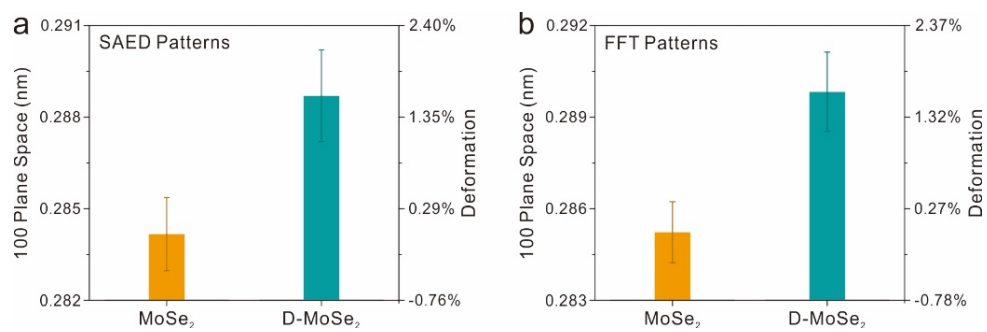
Figure S8. Statistical analyses of the (100) interplanar spacing values of the pristine $MoSe_2$ crystal and D-$MoSe_2$ crystal that extracted from the (a) SAED patterns and (b) FFT patterns. Both the results indicate a 1.5% amplification of the lattice after regulating the deformation recovery.
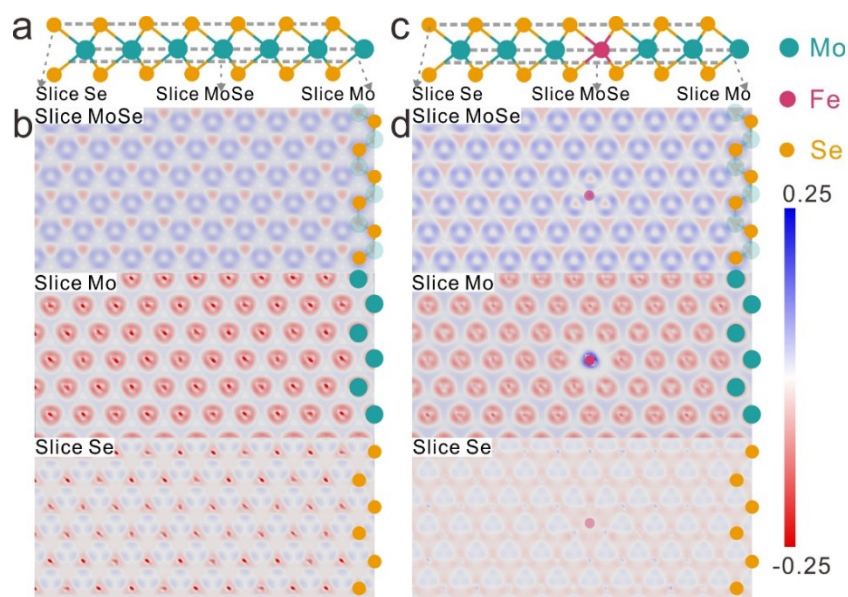
Figure S9. The side-view illustration of the analyzed (a) pristine MoSe$_2$ crystal and (c) D-MoSe$_2$ crystal. The corresponding isosurface images of the (b) pristine MoSe$_2$ and (d) D-MoSe$_2$ slices of the positions marked in (a) and (c), respectively. After Fe-doping, the charges at all the Se sites is increased and partial regions convert to the electron-trapping state.

For further investigating the MDD effect, the planar charge density difference slices acquired from the as-marked (001) plane of Mo–Se bonds (slice MoSe), the (001) plane of Mo atoms (slice Mo) and the (001) plane of Se atoms (slice Se) are analyzed. The side-view schemes of pristine MoSe$_2$ crystal and the D-MoSe$_2$ crystal are presented in Figure S9a and S9c, respectively, and the corresponding isosurfaces are exhibited in Figure S9b and S9d, respectively. The increase of charge density around the Mo and Se atoms among the entire cell could be confirmed. Moreover, it can also be convinced that the single Fe atom performed a uniform electron-donation effect on the whole 7×7 MoSe$_2$ crystal. In addition, the enlarged charge density of the Mo–Se bonds could be directly observed in the slice MoSe of D-MoSe$_2$ crystal (Figure S9b), in which the charge density is much larger (bluer) than that of pristine MoSe$_2$ crystal (Figure S9d).
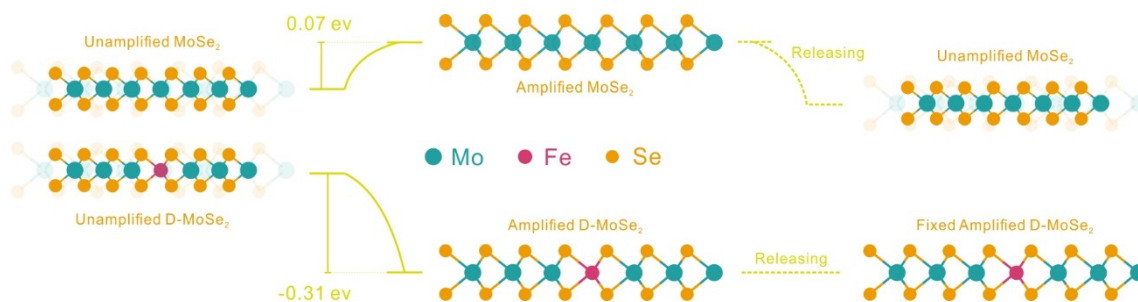
Figure S10. DFT calculations of the total energy of the 7×7 MoSe$_2$ crystals with the configurations of pristine lattice, 1%-amplified lattice, unamplified Fe-doping lattice and 1%-amplified Fe-doping lattice.

For further confirming the enhanced electrostatic repulsion between Mo–Se bonds of D-MoSe$_2$ crystal as well as the MDD effect, energy calculations of 7×7 MoSe$_2$ crystals with four configurations are performed. As exhibited in Figure S10, the energy of MoSe$_2$ crystal with 1% lattice amplification is 0.07 eV higher than that of the unamplified one. It indicates that the deformed lattice is thermodynamically unstable and it would recover to the original state spontaneously. However, the total energy of 1%-amplified D-MoSe$_2$ crystal is 0.31 eV lower than that of unamplified D-MoSe$_2$, which suggests the deformation recovery of D-MoSe$_2$ crystal could be eliminated. These results directly illustrate the regulation effect of deformed D-MoSe$_2$ lattice based on the MDD strategy.
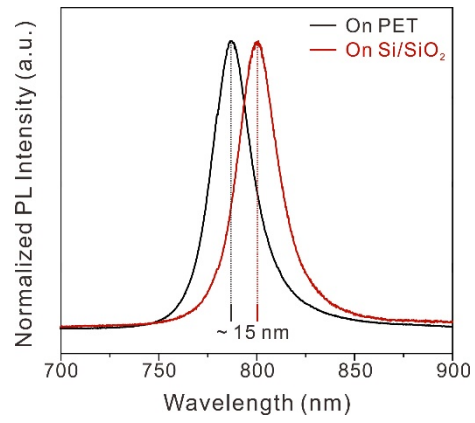
Figure S11. PL spectra of the pristine MoSe$_2$ crystal directly grown on Si/SiO$_2$ substrate (red line) and transferred on polyethylene terephthalate (PET) substrate (black line). A ~15-nm blue shift of the PL peak after transfer is indicated.
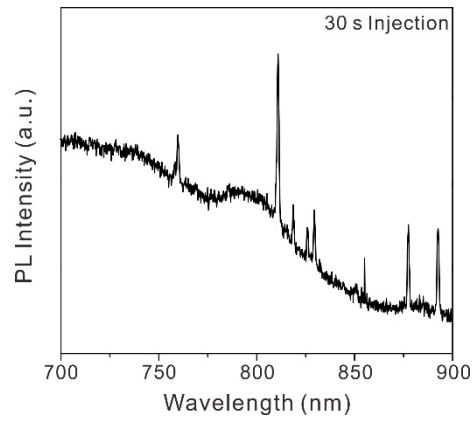
Figure S12. PL spectrum of the MoSe$_2$ crystal injected Fe ions for 30 s on PET substrate. No obvious PL signal is detected and the generated sharp peaks may drive from the Raman signals of PET substrate.
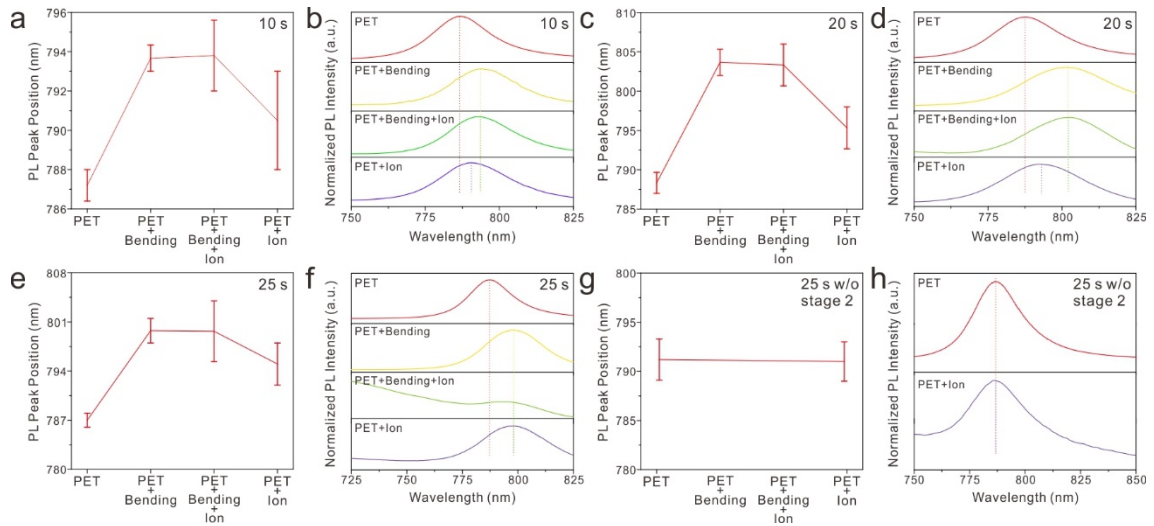
Figure S13. The statistical analyses of the PL peak position values at four stages that described in Figure 4a and the corresponding *in-situ* PL measurements of the MoSe$_2$ crystal for injecting Fe ions (a, b) 10 s, (c, d) 20 s, (e, f) 25 s in stage 3, and (g, h) 25 s without stage 2, respectively. All the results indicate the *in-situ* deformation-fixing effect based on the MDD strategy.

Figure S13 demonstrates the *in-situ* deformation-fix effect of the MDD strategy. The lattice deformation of MoSe$_2$ crystals resulted from the bending of PET substrates could be partially or fully fixed via doping metal donor atoms with appropriate amounts. No shift of the PL peak position is presented in the sample without bending and it reveals that the doping of heteroatoms would not lead to the variation of PL peaks as well as deformation in lattice.

TRANSPARENT METHODS

CVD Growth Procedure

The growth of monolayer $MoSe_2$ crystals utilized liquid glass as substrates, which is verified to be the promising substrate to realize the self-limited growth of 2D materials. Before growth, 30 mg Se powders with a purity of 99.95 wt.% and 15 mg MoO_3 powders with a purity of 99.9999 wt.% that purchased from Alfa Aesar China (Tianjin) Co. Ltd. was placed in the quartz tube via loading by quartz boats. Commercial soda-lime glass (1 cm × 1 cm) was employed as the growth substrate to achieve the D-$MoSe_2$ crystals via utilizing a corresponding metal foil as supporting substrate or to fabricate pristine $MoSe_2$ crystals via utilizing Si/SiO_2 as supporting substrate. For the growth of Au-doped $MoSe_2$ crystals, thermal evaporated Au layer (5 nm) on the glass substrate is utilized as the dopant and Si/SiO_2 is utilized as the supporting substrate. Most of the Au layer was pre-erased to expose the bare glass surface for a better growth. In this growth process, the glass was first heated to 1000 °C at an Ar gas flow rate of 150 sccm for maintaining 10 minutes in order to form a liquid glass plane. After cooling to 850 °C in 15 minutes, the MoO_3 powders began to be heated at ~750 °C and S powders at 150 °C for 10-minutes growth process with introducing 10 sccm H_2 to the chamber. After growth, the furnace was cooling to room-temperature naturally. The transfer of the samples to the Si/SiO_2 substrate or Cu grids was utilized the PMMA-assisted transfer method.

Characterization

Optical images were taken with an optical microscope (Olympus DX51) and AFM image was recorded in NT-MDT system via semicontact mode. Raman and PL spectra excited by a 532-nm laser were acquired in a micro-Raman spectrometer (Renishaw in Via) at room temperature. XPS spectra were performed on a Thermo Scientific, ESCALAB 250Xi via using monochromatic Al Kα radiation (225 W, 15 mA, 15 kV). The binding energies were calibrated by referencing the C 1s peak (284.8 eV). The TEM images were taken with an aberration-corrected, high-resolution TEM (FEI Titan Themis) operating at 80 kV. The HAADF-STEM images were taken with a JEOL (JEM-ARM300F) operating at 300 kV.

DFT Calculations

The DFT calculations of charge density difference were carried out via using the DMol^3 module[6] in the Materials Studio software (Bio Accelrys). The treatments of electron exchange and correlation energy are based on gradient-corrected Perdew-Burke-Ernzerh (GGA-PBE) function. The core electrons are treated with DFT semi-core pseudopotentials. The self-consistent-field (SCF) convergence criterion was set to be smaller than 10^{-5} Hartree in the calculation. A 7×7×1 Monkhorst-Packing grid was used to sample the Brillouin zone of the supercells. A space of 20 Å for the vacuum layer along the c axis is used to avoid the interaction between the layers.

SUPPLEMENTAL REFERENCE

1. Chen, J., Tang, W., Tian, B., Liu, B., Zhao, X., Liu, Y., Ren, T., Liu, W., Geng, D., Jeong, H.Y*., et al.* (2016). Chemical vapor deposition of high-quality large-sized MoS_2 crystals on silicon dioxide substrates. Adv. Sci. *3*, 1500033.

2. Feng, Q., Zhu, Y., Hong, J., Zhang, M., Duan, W., Mao, N., Wu, J., Xu, H., Dong, F., Lin, F*., et al.* (2014). Growth of large-area 2D $MoS_{2(1-x)}Se_{2x}$ semiconductor alloys. Adv. Mater. *26*, 2648–2653.

3. Zhang, J., Kang, W., Jiang, M., You, Y., Cao, Y., Ng, T.W., Yu, D.Y., Lee, C.S., and Xu, J. (2017). Conversion of 1T-$MoSe_2$ to 2H-$MoS_{2x}Se_{2-2x}$ mesoporous nanospheres for superior sodium storage performance. Nanoscale *9*, 1484–1490.

4. Yang, J., Chen, X., Ye, F., Wang, C., Zheng, Y., and Yang, J. (2011). Core-shell CdSe@Pt nanocomposites with superior electrocatalytic activity enhanced by lateral strain effect. J. Mater. Chem. *21*, 9088.

5. Li, Y., Zhang, K., Wang, F., Feng, Y., Li, Y., Han, Y., Tang, D., and Zhang, B. (2017). Scalable synthesis of highly crystalline $MoSe_2$ and its ambipolar behavior. ACS Appl. Mater. Interfaces *9*, 36009–36016.

6. Delley, B. (2000). From molecules to solids with the DMol3 approach. J. Chem. Phys. *113*, 7756–7764.